Tempering of Martensite in Dual-Phase Steels and Its Effects on Softening Behavior

V.H. BALTAZAR HERNANDEZ, S.S. NAYAK, and Y. ZHOU

The isothermal and nonisothermal tempering of martensite in dual-phase (DP) steels was investigated mainly by analytical transmission electron microscopy, and the effect on softening behavior was studied. The isothermal tempering resulted in coarsening and spheroidization of cementite and complete recovery of laths. However, nonisothermal tempering manifested fine quasi-spherical intralath and platelike interlath cementite, decomposition of retained austenite, and partial recovery of laths. The distinct characteristic of nonisothermal tempering was primarily attributed to the synergistic effect of delay in cementite precipitation and insufficient time for diffusion of carbon due to rapid heating that delays the third stage of tempering. The finer size and platelike morphology of cementite coupled with partial recovery of lath resulted in reduced softening in nonisothermal tempering compared to severe softening in isothermal tempering due to large spheroidized cementite and complete recovery of lath substructure. The substitutional content of precipitated cementite in nonisothermal tempering was correlated to the richness of particular steel chemistry. Softening resistance during nonisothermal tempering was related to DP steel chemistry, *i.e.*, Cr and Mn content. Fine cementite and less decomposed martensite in rich chemistry confer high resistance to softening compared to leaner chemistries, which indicated severe decomposition of martensite with coarser cementite.

DOI: 10.1007/s11661-011-0739-3

I. INTRODUCTION

DUAL-PHASE (DP) steel comprises a soft ferrite (α) matrix dispersed with hard martensite (α') phase to offer favorable combinations of high strength and good deformability, which has recently attracted an increasing application in automobile industries.[1] However, softening, reduction in hardness with respect to the base metal, of DP steel that occurs in a number of manufacturing processes, such as welding and joining[2,3] and laser heat treatment,[4] becomes an important issue that hinders the progress of implementing DP steel in many practical applications. For example, it is reported that softening occurring in the heat-affected zone (HAZ) caused by welding adversely affects the formability of tailor-welded blanks of DP steel due to high strain concentration in the softened region, leading to premature failure of the blanks.[5,6] HAZ softening was clearly linked to the tempering of α' phase in DP steel.[7–10]

In theory, tempering of martensite in DP steel occurs, just as tempering of fully martensitic steels,[11–13] when it is heated to temperatures close to or below lower critical transformation temperatures (Ac_1 line) irrespective of the manufacturing processes. The extent or degree of tempering (softening) fundamentally depends on diffusion of carbon and is controlled by two parameters, *i.e.*, temperature and time; accordingly, the tempering (softening) process can be divided into two categories: (1) isothermal tempering and (2) nonisothermal tempering. Isothermal tempering includes the conventional heat treatment process (slow heating, long holding time at peak temperature, and slow cooling) implemented in order to improve the ductility of steel (mostly martensitic steel),[11] whereas nonisothermal tempering occurs generally during manufacturing processes such as welding and joining involving rapid heating, negligible holding time at tempering temperature, and rapid cooling.

Tempering of martensite is well documented in the literature but has been mostly addressed to fully martensitic steels subjected to isothermal tempering treatment.[11–13] It is generally agreed that the tempering process is developed in a series of overlapped stages: the first stage (up to 523 K [250 °C]) involves clustering of carbon and precipitation of transition carbides, especially ε-carbides ($Fe_{2.4}C$);[11,14] in the second stage, 473 K to 573 K (200 °C to 300 °C), retained austenite, if any, decomposes to form α and Fe_3C (cementite);[15–17] and, in the final stage, *i.e.*, above 523 K (250 °C) cementite coarsens and forms spheroids[18,19] followed by recovery or recrystallization of martensite above 873 K (600 °C).[20,21] However, there is little work on detailed tempering behavior, such as carbide precipitation

---

V.H. BALTAZAR HERNANDEZ, formerly Graduate Student with the Mechanical and Mechatronics Engineering, University of Waterloo, Waterloo, ON N2L 3G1, Canada, is now Professor with the MpyM-EPMM Academic Unit of Engineering, Autonomous University of Zacatecas, C.P. 98000 Zacatecas, Mexico. S.S. NAYAK, Postdoctoral Fellow, is with the Centre for Advanced Materials Joining, University of Waterloo, is also with the Mechanical and Mechatronics Engineering, University of Waterloo. Contact e-mail: sashank@uwaterloo.ca Y. ZHOU, Director, is with the Centre for Advanced Materials Joining, University of Waterloo, and is also a Professor with the Mechanical and Mechatronics Engineering, University of Waterloo.

Manuscript submitted December 23, 2010.

and recovery and its influence on softening, of DP steel and also very little on nonisothermal tempering of fully martensitic steels. Most publications on DP steels were on the effects of softening on mechanical performance, such as formability, and tensile and fatigue properties,[5–10,22] with some preliminary work on the effects of steel chemistry on softening.[23]

Because of the negligible holding time, nonisothermal tempering is strongly affected by the heating rate. For example, it has been reported that diode laser welding produced much more severe softening because of its slower heating rate, compared to Nd:YAG laser welding.[7] According to work on induction heating rates, which may be the only open literature on nonisothermal tempering of fully martensitic steel,[24] increasing the heating rate would result in refinement of cementite particles.[25] This was ascribed to the increased temperature required for cementite precipitation and higher nucleation rate of cementite during rapid heating.[24] Furthermore, delay in commencement of cementite spheroidization to 873 K (600 °C) was also observed during rapid heating, which compares to the effects at lower temperatures, *e.g.*, 773 K (500 °C) in slow heating.[26]

The objectives of the present work are to study the characteristics of martensite tempering in DP steels subjected to both isothermal and nonisothermal tempering and its effect on softening behavior. In addition, the influence of DP steel chemistry on tempering behavior and eventually on softening was studied.

Table I. Chemistry of DP Steels (Weight Percent): CE Was Used to Categorize the DP Steels

	Steel		
Element	DP_L	DP_M	DP_R
C	0.150	0.132	0.147
Mn	1.500	1.907	1.719
P	0.010	0.014	0.013
S	0.006	0.006	0.002
Si	0.313	0.030	0.294
Cu	0.021	0.036	0.039
Ni	0.010	0.019	0.040
Cr	0.021	0.161	0.612
Sn	0.009	0.007	0.002
Mo	0.006	0.036	0.018
Al	0.047	0.058	0.036
Nb	0.002	0.003	0.004
Ti	0.002	0.002	0.007
V	0.003	0.005	0.008
N	0.009	0.009	0.006
CE	0.390	0.475	0.525

II. EXPERIMENTAL PROCEDURE

The starting materials in this study were three zinc-coated 1.2-mm-thick DP steel sheets. Table I categorizes the DP steels according to their alloying level and, in turn, carbon equivalent (CE) calculated using Yurioka formula[27] as lean (DP_L), moderate (DP_M), and rich (DP_R). Furthermore, the mechanical properties and volume fraction of martensite of the DP steels are listed in Table II. The volume fraction of martensite (f_m) was measured by standard metallographic analysis. Assuming that the microstructure consists of only ferrite and martensite of equal density, the martensite carbon content was calculated using the established equation:[28,29]

$$|\text{pct C}|_m = \frac{|\text{pct C}|_a - |\text{pct C}|_f\,(1 - f_m)}{f_m} \qquad [1]$$

where $|\text{pct C}|_m$, $|\text{pct C}|_f$, and $|\text{pct C}|_a$ are carbon contents (weight percent) of martensite, ferrite, and bulk steel, respectively, and f_m is the volume fraction of martensite. Calculations were obtained by assuming a carbon content of 0.005 pct in ferrite at room temperature.[30] The mechanical properties (Table II) correlate well to the fraction of α' phase in the DP steels.

Figure 1 compares the thermal cycles for nonisothermal and isothermal tempering implemented on the DP steels in the present study. Isothermal tempering was carried out in a muffle furnace with very low heating rate (0.5 K/s), followed by longer holding times (t = 5300 and 5400 seconds) at 923 K (650 °C) and cooling from

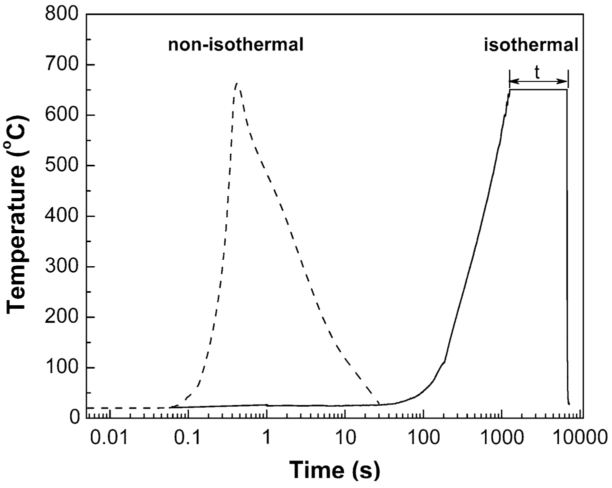

Fig. 1—Thermal cycle of nonisothermal and isothermal tempering implemented on DP steels.

Table II. Base Metal Properties of DP Steels

Steel	f_m	Calculated α'-Carbon Content (Wt Pct)	Hardness (HV)	0.2 Pct YS (MPa)	UTS (MPa)	Total Elongation (Pct)
DP_L	54	0.273	330	674	1061	12
DP_M	48	0.269	301	534	979	15
DP_R	40	0.360	281	524	820	18

peak to room temperature in around 10 seconds by air cooling. Nonisothermal tempering was achieved by resistance spot welding because of its far-from-equilibrium nature compared to other welding processes, and the experimental details of the process were reported elsewhere.[31] The nonisothermal tempering cycle plotted in Figure 1, based on a numerical simulation of the thermal cycle at a weld location experiencing a peak temperature of about 923 K (650 °C),[31] involves rapid heating (>2000 K/s), negligible holding time (milliseconds) at peak temperature, followed by fast cooling (≈60 K/s) to room temperature. It should be noted that due to the presence of strong magnetic fields generated during the process, it is difficult to obtain the peak temperature distribution experimentally in RSW. Hence, a numerical simulation was adopted in the present work in order to estimate the peak temperature gradient along the subcritical HAZ, the details of which are reported in the authors' earlier work.[31]

The cross section of resistance-spot-welded DP steel was comprised of different zones of a weldment, *i.e.*, the fusion zone, the base metal (BM), and the HAZ, which was subdivided at the location of Ac_1 as upper-critical HAZ and subcritical HAZ; the details are reported elsewhere.[31,32] Phase analysis of the BM and isothermally tempered specimens was carried out in a RIGAKU* micro-XRD diffractometer equipped with Cu radiation (λ = 1.5405 Å). The microstructures of the subcritical HAZ and BM of the different DP steels were analyzed using a JEOL7000F** scanning electron microscope (SEM) and a PHILIPS CM12† transmission electron microscope (TEM) operated at 120 kV. The compositions of carbides were analyzed using a TEM with energy-dispersive X-ray spectroscopy (EDX). The average carbide size was determined from TEM and SEM images by taking at least 30 measurements from several fields of view of different magnifications. In the case of irregular shape, the minimum length (elongated) or diameter (quasi-spherical shape) of the examined particle was considered as the carbide diameter.[12] A SHIMADZU HMV-2000‡ hardness tester was used to measure Vickers microhardness on mounted, polished, and etched specimens using a load of 200 g with 15 seconds of dwell time keeping 200-μm spacing between subsequent indentations.

Specimens for XRD, SEM, and hardness study were prepared by mechanical grinding and polishing using standard metallographic techniques followed by etching with 1 pct nital solution (1 pct HNO_3 and 99 pct ethanol) for 8 to 10 seconds. TEM samples were prepared by three different techniques, *viz*. focused ion beam (FIB), standard twin-jet electropolishing, and carbon extraction replicas. As locations of interest were generally too small, a lift-out FIB technique for extracting TEM samples was used for the nonisothermally tempered specimen from the welds, and FIB sampling of BM was also done for effective comparison. The location of FIB sampling was kept at 100 μm outside of the Ac_1 line at the subcritical HAZ, because this location attains temperature ~923 K (650 °C) in welds.[31] Initially, carbon film was deposited on the subcritical HAZ zone, after which a milling process was started by shaping a thin lamella within the bulk specimen, and then the specimen was fully shaped and cut followed by lifting-out the specimen using a micromanipulator. Finally, the lift-out specimen was attached to a Cu grid holder and further milling for thinning was performed. The twin-jet electropolishing technique was adopted for preparing samples from isothermally tempered DP steel. Specimens were mechanically ground to prepare thin foils (70 to 80 μm), which were punched to make 3-mm-diameter discs. The discs were then thinned in a STRUERS TENUPOL-5§ twin-jet electropolishing unit using 10 pct $HClO_4$ and 90 pct ethanol containing electrolyte maintained at –45 °C, maintaining a voltage of 15 V. Carbon extraction replicas were prepared for structural analysis of the precipitated carbides in nonisothermally tempered specimens. After masking the nondesirable regions in the specimen etched with 1 pct nital solution, a thin carbon film was deposited. The carbon film was then floated off in a solution of 4 pct nitric acid in ethanol and collected onto carbon-coated Cu grids.

III. RESULTS AND DISCUSSION

Tempering of martensite and carbide precipitation analysis in DP steel subjected to isothermal and nonisothermal tempering is reported first with main focus on DP_M steel; whereas results of DP_L and DP_R steels are discussed subsequently to clarify the effect of DP steel chemistry on nonisothermal tempering characteristics and softening behavior.

A. *Base Metal Microstructure of DP_M Steel*

Representative SEM micrographs (Figures 2(a) and (b)) showed that the base metal (BM) microstructure of

---

*RIGAKU is a trademark of Rigaku Corporation, Tokyo.

**JEOL7000F is a trademark of Japan Electron Optics Ltd., Tokyo.

†PHILIPS CM12 is a trademark of Royal Philips Electronics, Amsterdam.

‡SHIMADZU HMV-2000 is a trademark of Shimadzu Corporation, Kyoto.

§STRUERS TENUPOL-5 is a trademark of Struers, Ballerup, Denmark.

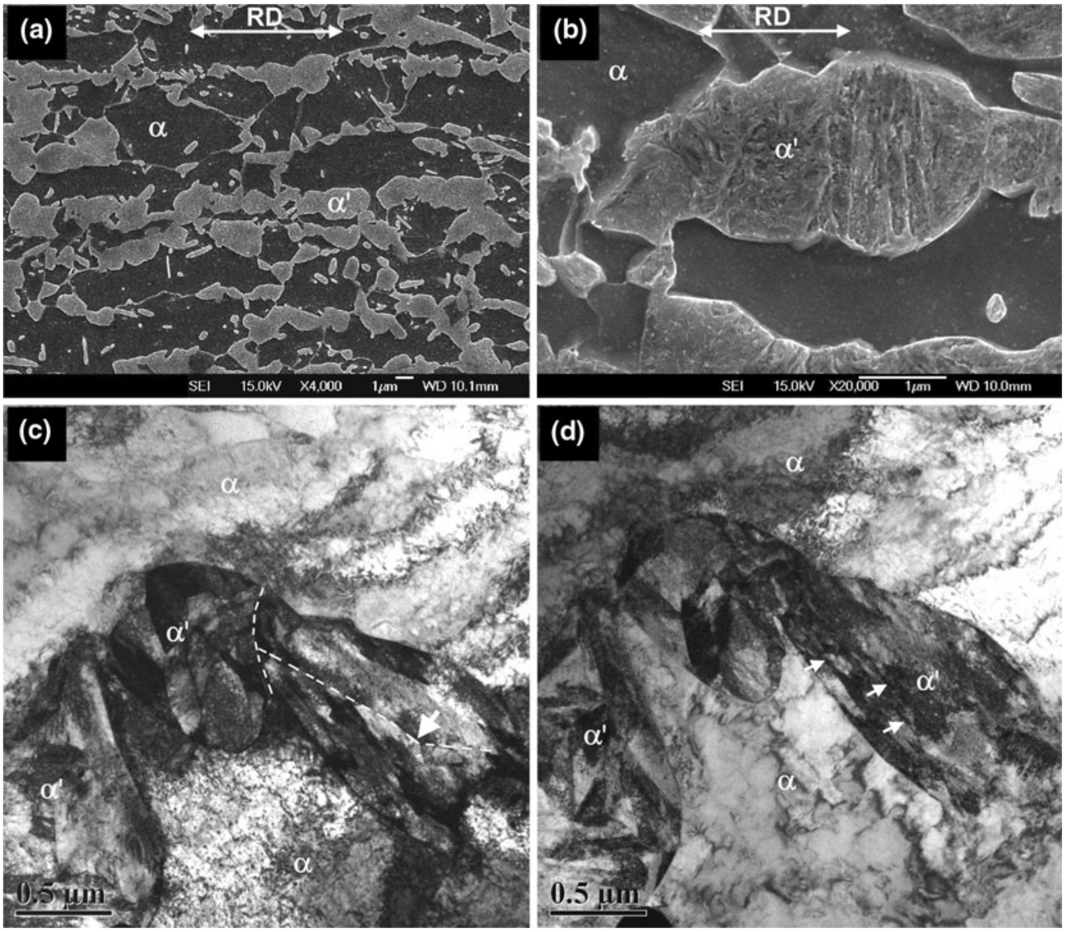

Fig. 2—Microstructure of DP_M steel BM: SEM micrographs showing (*a*) ferrite α-matrix along with banded islands of martensite (α′), (*b*) substructure within α′ phase, and (*c*) and (*d*) TEM bright-field images taken at two tilt angles illustrating α′ phase and α matrix.

DP_M steel (Table I) comprises dark ferrite matrix (α) along with gray banded islands of martensite (α′) aligned parallel to the rolling direction (marked in Figures 2(a) and (b)) of the sheet. The solid featureless appearance of α′ phase (Figure 2(a)) actually contains lathy substructure, as depicted in Figure 2(b). TEM bright-field images taken at two tilt angles (Figures 2(c) and (d)) distinctly delineated the microstructural features, *i.e.*, random arrays of dislocations in the α matrix, α′ phase, prior-γ grain boundaries (α/α′ boundaries), and block boundaries (marked by white dotted line), which separate α′ blocks containing parallel laths (arrows in Figure 2(d)). Hereafter, high-angle boundaries will be identified as prior γ grain boundaries and block boundaries and low-angle boundaries as lath boundaries. The presence of lath substructure indicated that DP_M steel contains low-carbon α′, which is supported by its carbon content (0.269 wt pct), as given in Table II. It is reported that low-carbon martensitic steel microstructure is characterized by different structural units within prior-γ grains, *viz*. packets that are the larger or higher units comprise blocks (lower units) containing parallel martensite laths (lowest units).[24,33] Hence, it was concluded that α′ phase in the DP_M steel has microstructural features similar to low-carbon martensitic steel. Furthermore, a high density of dislocations, a typical characteristic feature of low-carbon martensite laths,[34] was also observed in the high-magnification image, which is reported elsewhere.[32]

In addition to α matrix and α′ phase, a small fraction of retained austenite was observed along the lath boundaries (interlath) in the BM of DP_M steel, as delineated by a bright-field image (Figure 3(a)) and further confirmed by a dark-field image (Figure 3(b)) taken using the $(\bar{3}\bar{3}1)$ spot of austenite (arrow in Figure 3(c)). The selected area diffraction (SAD) pattern of the region in Figure 3(a) and its indexing are illustrated in Figures 3(c) and 3(d), respectively. Diffraction spots from $[\bar{1}13]_{\alpha'}$ and $[\bar{2}33]_{\gamma}$ zone axes of α′ phase and retained austenite were obtained, indicating an orientation relationship of $[\bar{1}13]_{\alpha'}//[\bar{2}33]_{\gamma}$. It is known that interlath retained austenite generally forms in medium- and high-carbon martensite in fully martensitic steels.[15,16] However, Mn is reported to promote the formation of interlath retained austenite in steel.[35] Thus, despite the low-carbon content in α′ (Table I), Mn content was concluded to be sufficient to stabilize the interlath austenite within martensite laths in DP_M steel.

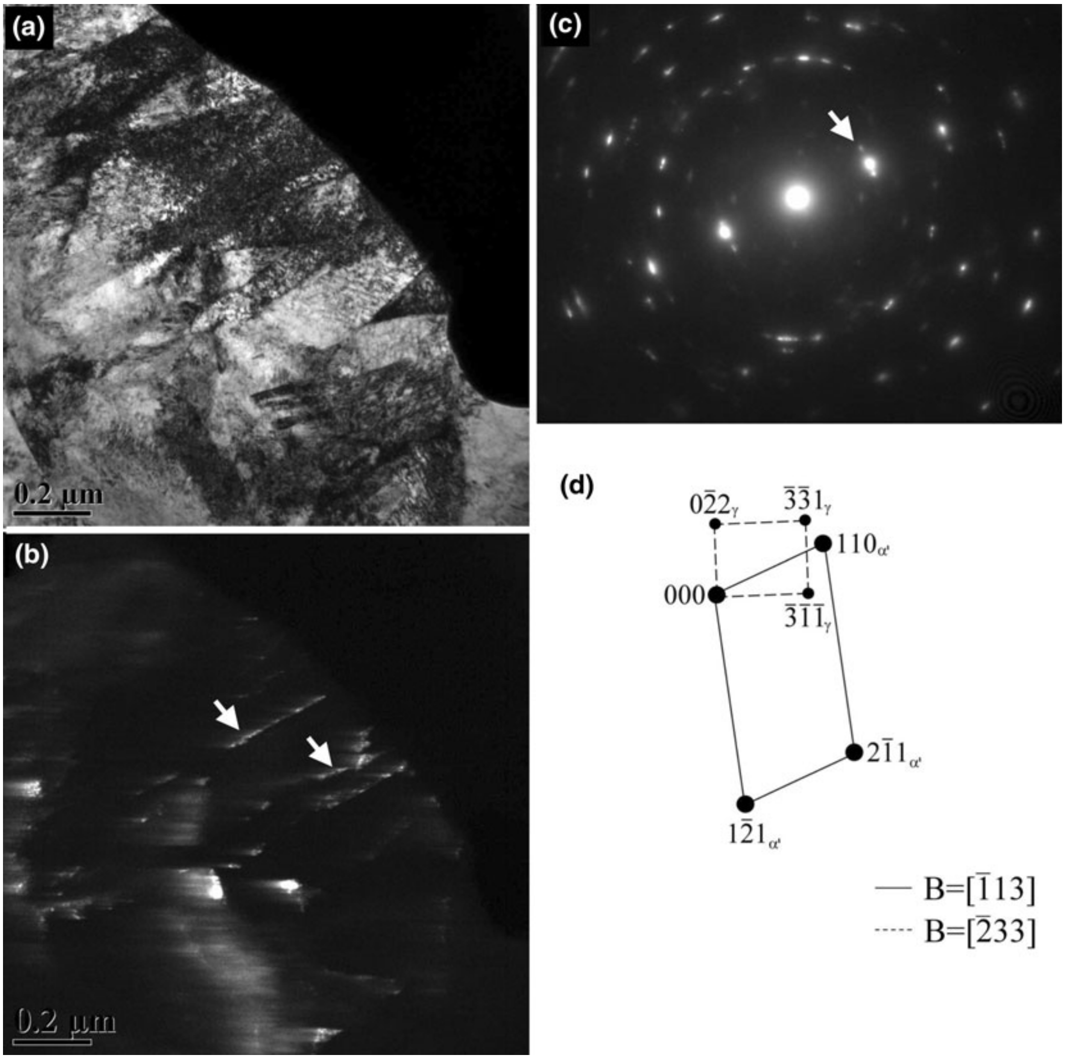

Fig. 3—Interlath retained austenite in BM of DP_M steel: (*a*) bright-field and (*b*) dark-field images taken using $(\bar{3}\bar{3}1)_\gamma$ reflection, (*c*) SAD pattern of (a), and (*d*) schematic of SAD pattern indexing.

B. *Isothermal Tempering of DP_M Steel*

Figure 4 depicts representative SEM and TEM micrographs of the isothermally tempered DP_M steel. The banded morphology of the parent α' phase (Figure 2(a)) was still seen in Figure 4(a), but was severely decomposed, containing a high density of precipitated carbides uniformly distributed throughout, indicating the tempered martensite (TM) structure. The high-magnification image (Figure 4(b)) indicated that larger carbides are located at prior-γ grain boundaries and block boundaries. This was further confirmed by bright-field images taken at two tilt angles (Figures 4(c) and (d)), which also illustrated recovery of martensite as confirmed by the SAD pattern showing $[\bar{1}33]_\alpha$ zone axis and precipitation of finer carbides within recovered structure (marked by arrows). Recovery in isothermal tempering was further corroborated by extensive reduction in dislocation density and complete disappearance of the prior lath boundaries (Figures 4(c) and (d)). However, recrystallization was not detected, which was confirmed by the presence of prior-γ grain boundaries with the banded morphology (Figures 4(a) and (b)). Bright-field micrographs of precipitated carbides located at the edge of an electropolished specimen of isothermally tempered DP_M steel are delineated in Figures 5(a) and (b). The SAD pattern taken from one of these carbides (circled region in Figure 5(b)) indicated diffraction spots from the [010] zone axis of orthorhombic cementite (θ) (Figure 5(c)). The dark-field image of the carbide (Figure 5(d)) taken using (200) reflection further confirmed the precipitation of cementite in isothermally tempered DP_M steel corroborating well with the XRD analysis.[32] It should be noted that the XRD patterns of the DP_M steel BM showed peaks typical of bcc structure corresponding to the α matrix, whereas specimens isothermally tempered at 923 K (650 °C) for 300 seconds resulted in new peaks of the orthorhombic crystal structure of cementite and the number of which increased with time (5400 seconds), suggesting an increase in volume fraction of cementite.[32]

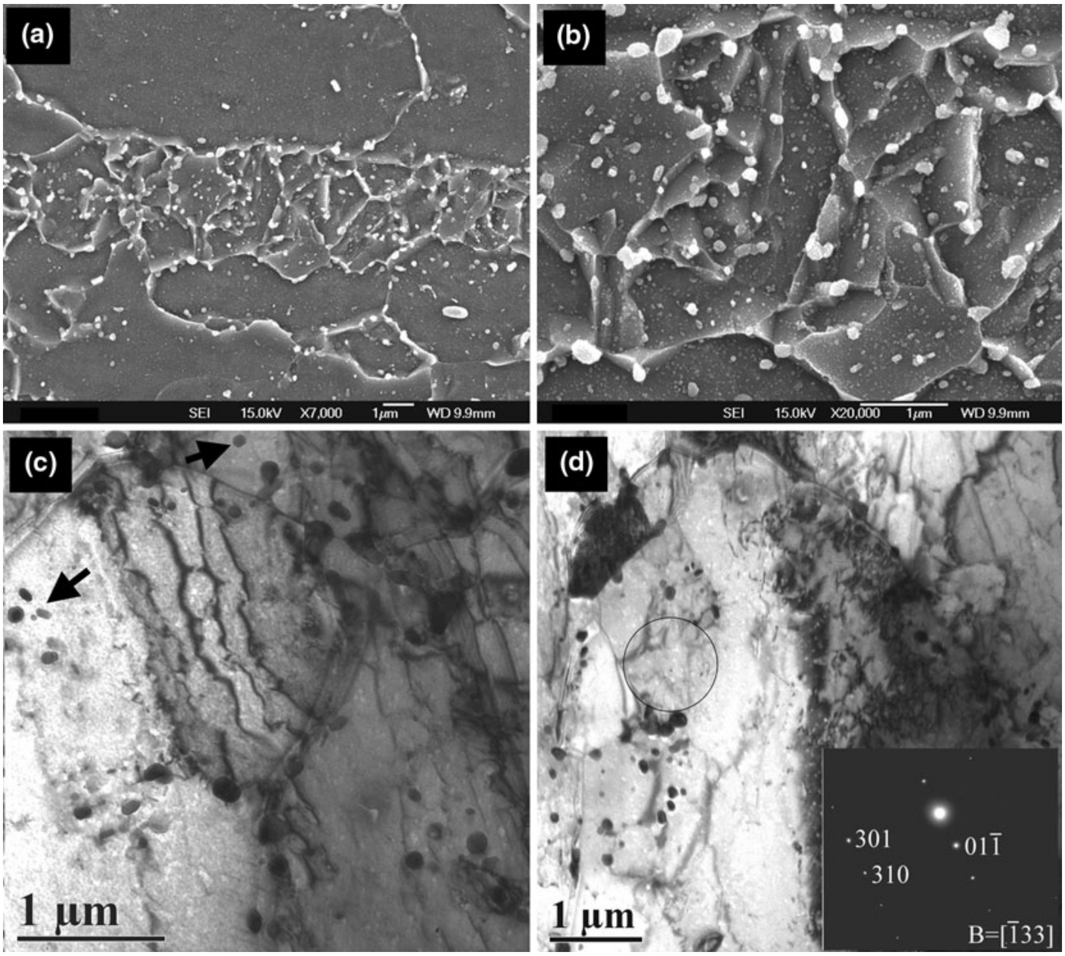

Fig. 4—DP$_M$ steel isothermally tempered at 923 K (650 °C) for 5400 s: SEM micrographs showing (*a*) decomposition of the prior α' phase, (*b*) precipitated carbides predominantly located at the grain boundaries, and TEM observations at two tilt angles showing (*c*) carbide precipitation within the tempered structure and (*d*) recovery of the lath boundaries. Inset SAD pattern in (d) indicates bcc structure (α) of tempered matrix.

Since the DP$_M$ steel was characterized by the presence of low-carbon martensite laths (Figures 2(c) and (d)), it is interesting to note that the tempered structure of DP$_M$ steel (Figure 4) is similar to that of the low-carbon martensitic steels subjected to similar isothermal tempering temperature.[36,37] For instance, tempering of low-carbon martensitic steels at high temperature, *i.e.*, 923 K (650 °C), is characterized by coarsening and spheroidization of cementite (mainly located at grain boundaries) and extensive recovery of the lath structure with formation of elongated or equiaxed α grains.[20,21] The recovery process is usually associated with migration of boundaries containing relatively low dislocation density (*i.e.*, lath boundaries) and dislocation cells toward higher dislocation density boundaries, *i.e.*, block and prior-γ grain boundaries, which results in complete disintegration of the laths.[20,38,39] Hence, it was concluded that the complete recovery of the lath boundaries observed in isothermally tempered DP$_M$ steel (Figures 4(a) through (d)) is related to migration or disintegration of the prior lath boundaries. Furthermore, low-carbon martensitic steels are reported to have stable structure against recrystallization despite having high dislocation density due to obstruction of dislocation movement by carbides,[20,37] which supports the absence of recrystallization in the TM structure of DP$_M$ steel.

C. *Nonisothermal Tempering of DP$_M$ Steel*

1. *Characteristics of carbide precipitation*

SEM micrographs (Figures 6(a) and (b)) of nonisothermally tempered DP$_M$ steel clearly depicted the α matrix (dark regions) along with decomposed lathy morphology (gray regions) typical of TM in contrast to severely decomposed isothermal TM (Figures 4(a) and (b)) and solid morphology of α' phase in the BM (Figures 2(a) and (b)). Furthermore, nonisothermal tempering resulted in fine decoration of submicron particles (white) along the prior-γ grain boundaries, block boundaries, and interlath regions in TM (Figure 6(b)) in contrast to coarser precipitates only at prior-γ grain boundaries and block boundaries in isothermal tempering (Figure 4(b)). Also, the rounded carbides (white) within blocks in nonisothermal tempering were finer than carbides within the block in isothermal tempering. Bright-field images of nonisothermally tempered DP$_M$ steel at two tilt angles (Figures 6(c) and (d)) indicated clearly the prior-γ grain boundaries,

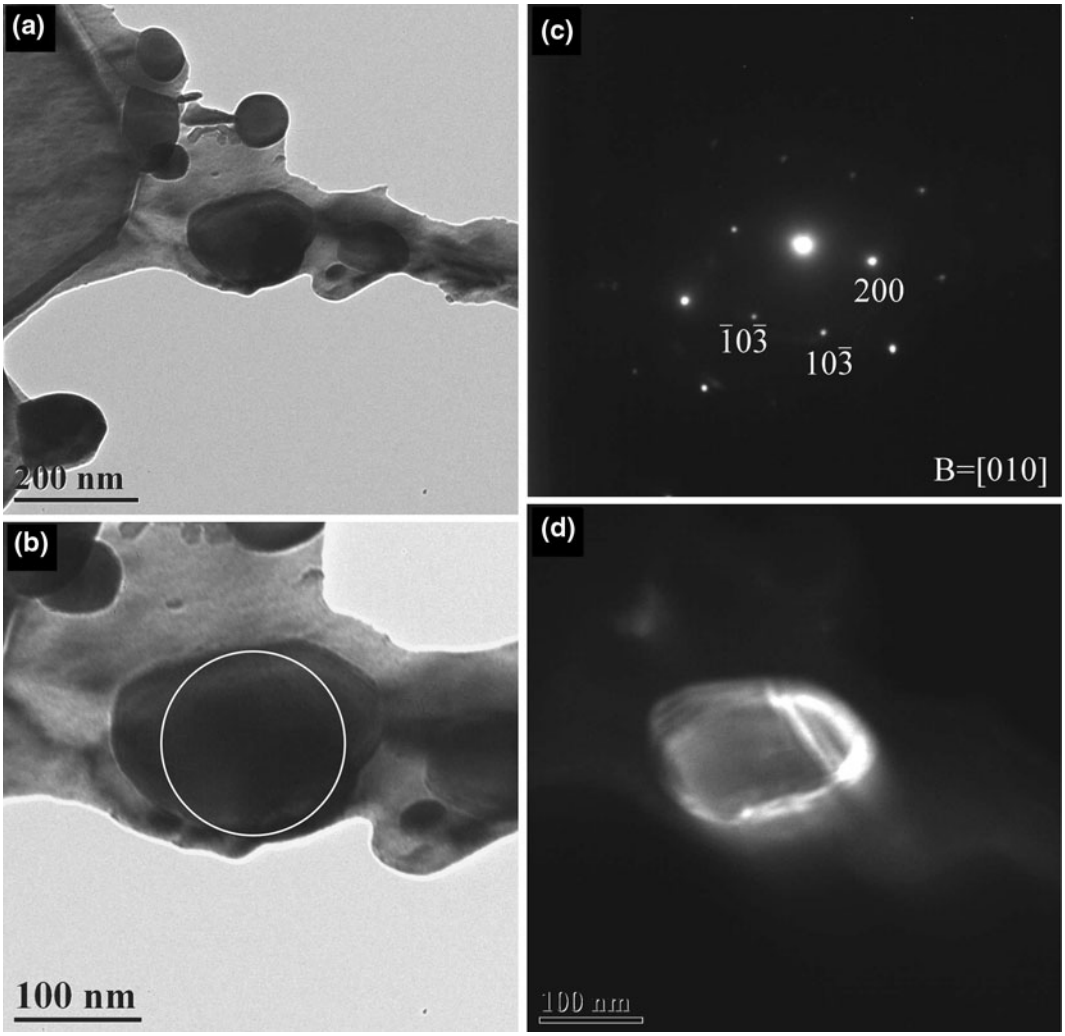

Fig. 5—DP_M steel isothermally tempered at 923 K (650 °C) for 5400 s illustrating (*a*) carbide precipitation, (*b*) high magnification image of the precipitated carbide, (*c*) SAD pattern confirming orthorhombic structure of cementite (θ), and (*d*) DF imaging taken using (200) reflection of cementite.

residual α'-lath morphology containing high dislocation densities, and precipitation of carbides (marked by arrows) within the TM matrix.

Bright-field images of the TM region clearly illustrated the carbides precipitated along the lath boundaries (interlath) and within laths (intralath) (Figures 7(a) and (b)). High-magnification images (Figures 7(c) and (d)) suggested that intralath carbides have irregular morphology, whereas interlath carbides have platelike morphology (Figure 7(b)). Furthermore, bright-field images of extracted replicas of nonisothermally tempered DP_M steel depicted a quasi-spherical morphology of carbides (Figures 8(a) and (b)). The indexing of SAD patterns (Figure 8(c)) of quasi-spherical carbide indicated diffraction spots from the [010] zone axis of orthorhombic structure confirming precipitation of cementite, which was further supported by the dark-field image (Figure 8(d)) taken using (101) reflection. Another interesting aspect of the nonisothermally tempered structure was precipitation of elongated interlath carbides in low volume fraction (arrows in Figures 9(a) through (c)), which were confirmed to be cementite by the SAD pattern (circled region in Figure 9(c)), illustrating a composite diffraction pattern with spots from cementite (c) and α matrix, showing the $[012]_{\alpha}//[101]_{c}$ orientation relationship (Figure 9(d)). Elongated cementite observed was an indication of interlath retained austenite in the parent α' in the BM (Figure 3), which transformed during nonisothermal tempering to form α and cementite. It may be recalled that interlath elongated cementite was not seen in the isothermally tempered DP_M steel (Figures 4 and 5).

The comparison of isothermally and nonisothermally tempered DP_M steel indicated a clear difference in the size, morphology, and locations of precipitated cementite in both TM structures. Table III compares the average cementite size at different locations in isothermally and nonisothermally tempered DP_M steel. For instance, the size of interlath and intralath cementite (~22 nm) in nonisothermally TM (Figures 6 and 8) was finer compared to cementite precipitated within blocks (~110 nm) in isothermal tempering. The precipitation of interlath cementite (Figure 7(b)) clearly indicated the persistence of the lath structure in nonisothermally

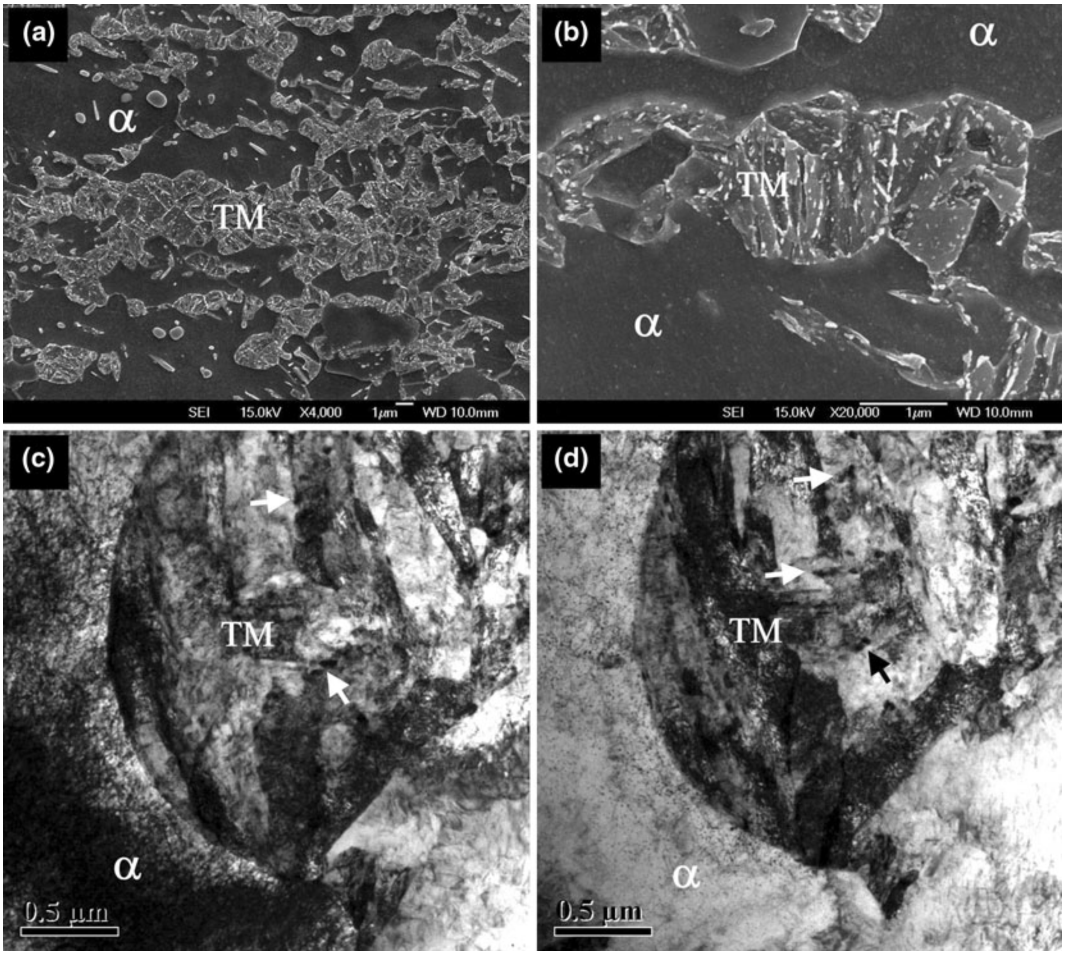

Fig. 6—SEM and TEM observations of nonisothermally TM in DP_M steel: (*a*) overall view, (*b*) details of the TM region, and (*c*) and (*d*) BF images at two different tilt angles showing carbide precipitation along interlath boundaries.

tempered DP_M steel. A significant reduction in dislocation density associated with the higher population of cementite unveiled that precipitation of cementite took place at dislocations during nonisothermal tempering (Figure 7(b)). Furthermore, precipitation of large spheroidized cementite (~225 nm) at prior-γ grain boundaries and block boundaries in isothermally TM (Figures 4 through 6) was in contrast to the fine cementite (~45 nm) at the same locations of nonisothermally TM. It may be mentioned that the white particles observed in SEM images of both TM structures (Figures 4(b) and 6(b)) actually correspond to the precipitated cementite, as confirmed by TEM analysis (Figure 5 and 7). The main aspect of nonisothermal tempering was the significant refinement of cementite particles compared to that in isothermal tempering (Table III).

A similar trend in size and locations of precipitated cementite by rapid heating in tempering of martensitic steel was also reported.[24,25] Corroborating the present work, Furuhara *et al.* also reported difference in locations of cementite precipitation in nonisothermal and isothermal tempering at 923 K (650 °C).[24] In nonisothermal tempering, finer cementite precipitated within laths and interlath regions compared to that at prior-γ and block boundaries, whereas isothermal holding (3600 seconds) resulted in growth of the cementite at all locations, but the trend in cementite size at location remained similar. Comparing the size of cementite in the present work (interlath and intralath: 22 nm, block/prior boundaries: 45 nm) and that reported by Furuhara *et al.*[24] (at low-angle boundaries: 12 nm, along high-angle boundaries: 15 nm) indicated that cementite in the present work is coarser. This may be because DP_M steel has lean chemistry, whereas the steel of Furuhara *et al.*[24] has high carbon and Cr content, which restricts growth of the cementite in tempering.[25]

From the aforementioned locations and size of cementite in both the tempered structures of DP_M steel, it was concluded that precipitation of cementite is controlled by diffusion of carbon atoms to lattice defects in the following order: prior-γ grain boundaries and block boundaries (larger cementite), lath boundaries (fine interlath cementite), and dislocations (finer intralath cementite). This finding is very consistent with earlier reports on isothermal tempering of low-carbon martensite describing cementite precipitation in the early stages of tempering and its consequent coarsening at the same locations by increasing temperature.[36,37]

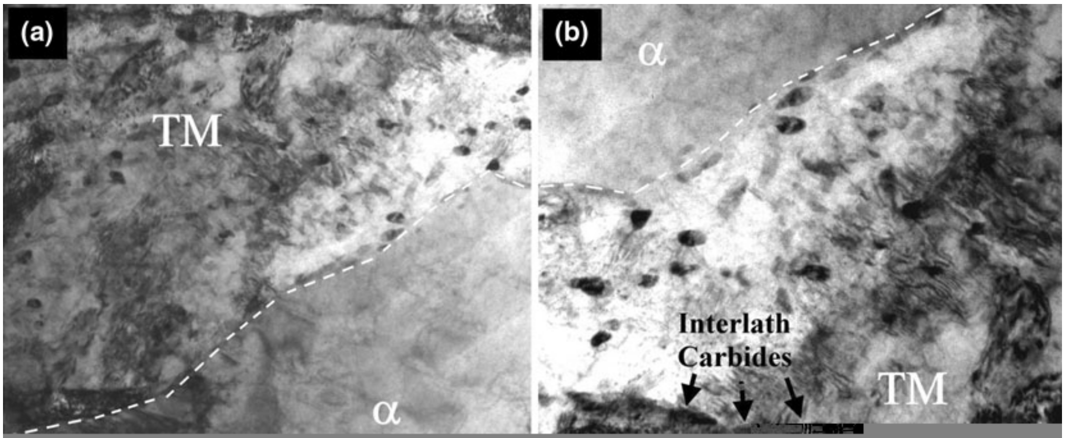

Fig. 7—BF images of the TM substructure in nonisothermal tempering showing (*a*) an overview of the α-TM interface, (*b*) interlath carbide precipitation, and (*c*) detailed observation of the precipitated intralath carbides. (*d*) High magnification showing carbide morphology in (c).

2. *Partial recovery of the martensite laths*

In addition to formation of refined cementite, nonisothermal tempering of DP_M steel resulted in partial recovery of α' laths (Figure 10), as confirmed by reduced dislocation density in the lath substructure (white dashed line in Figure 10(a)) compared to the surrounding matrix.[40] Higher magnification image (Figure 10(b)) indicated possible migration of lath boundaries (pointed by arrows) of the prior α'-phase toward block boundaries. However, the lath boundary migration process was seen to be incomplete due to lack of sufficient time available in nonisothermal tempering. Partial recovery of the lath substructure in nonisothermally TM was a distinct finding compared to complete recovery in isothermal tempering (Figure 4). The kinetics of recovery of the lath structure during tempering is generally influenced by two important factors: suppression of disintegration or migration of the lath boundaries (pinning effect) by carbides,[20] and gradual development of recovery of lath structure with time.[40] Thus, it was concluded that partial recovery in nonisothermal tempering of DP_M steel is a combined effect of retarding of lath boundary migration to block boundaries by fine precipitated cementite (Table III) and insufficient time available for the development of recovery processes. Furthermore, the morphology of the precipitated carbides plays an important role in the recovery process;[38,40] *e.g.*, the interlath platelike cementite (Figure 7(b)) delays the recovery process in nonisothermal tempering by impeding the movement of dislocations by a pinning effect.[39,40]

The precipitation and growth mechanism of cementite during isothermal and non-isothermal tempering of DP_M steel is illustrated by the schematic in Figure 11, which also indicates the difference in recovery of lath substructure in both tempering processes. The important differences of the TM structure in nonisothermal tempering compared to isothermally tempered DP_M steel are as follows: (1) finer cementite despite short holding time: intralath cementite is quasi-spherical, whereas interlath cementite adopts a platelike morphology; (2) decomposition of interlath retained austenite to

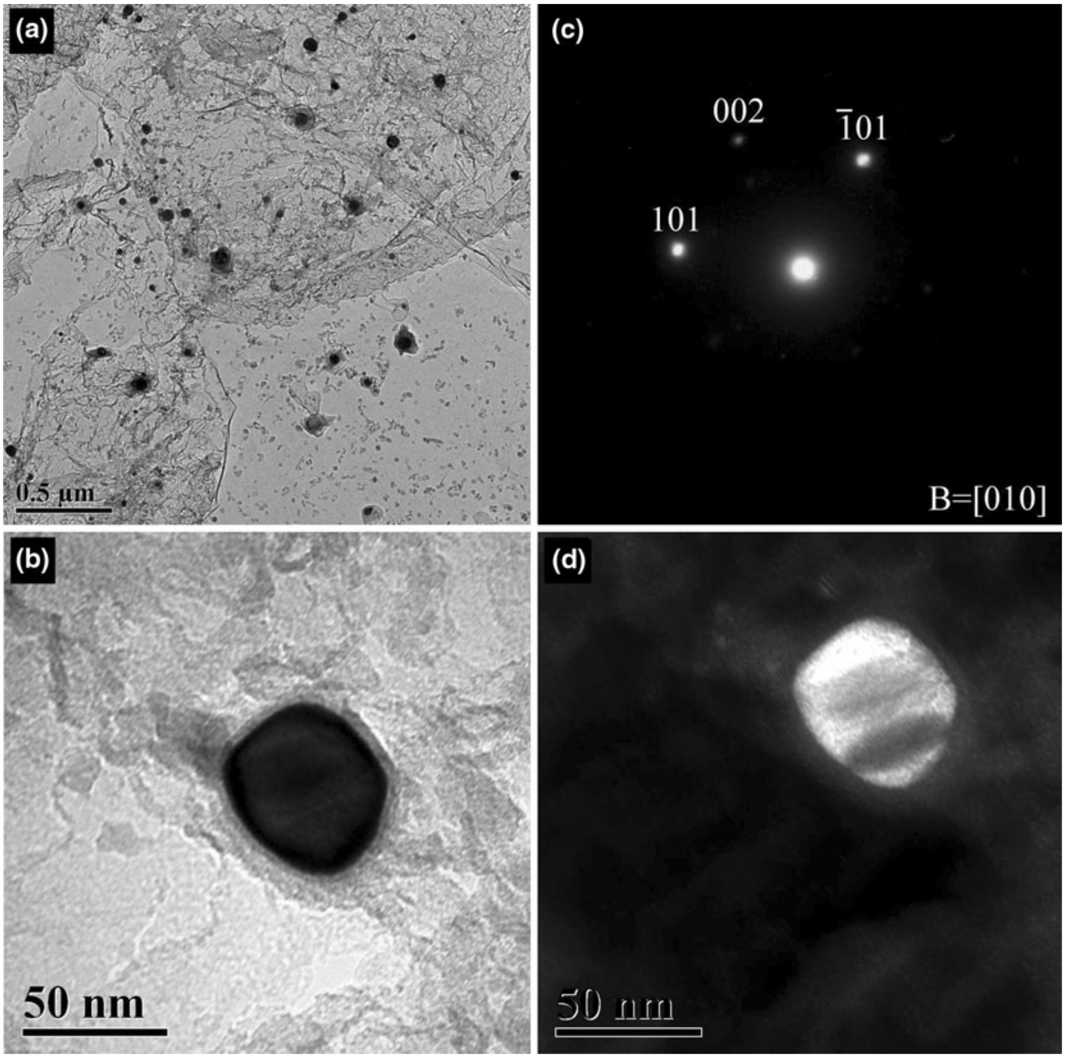

Fig. 8—TEM images of nonisothermally tempered DP_M steel showing (*a*) extracted replicas containing carbides, (*b*) quasi-spherical morphology of single carbide, (*c*) SAD pattern showing orthorhombic structure of carbide, and (*d*) dark-field image taken using (101) reflection of cementite.

form elongated cementite; and (3) partial recovery of the martensite lath substructure owing to reduced lath boundary migration. Another interesting aspect was that various tempering reactions, which take place during the conventional high-temperature (third stage) tempering of martensite, were easily delayed in nonisothermal tempering, *i.e.*, coarsening and spheroidization of the precipitated carbides, and complete recovery of lath substructure, which is consistent with earlier reports on low-carbon martensitic steel.[24–26]

3. *Coarsening kinetics of cementite*

The coarsening of cementite particles occurs by the diffusion of solute atoms down the concentration gradients in the matrix and can be predicted by a power-law relationship:[41]

$$r = k \times t^n \qquad [2]$$

where r is the radius of cementite at time t; k is the coarsening rate constant, which is a function related to the solubility, boundary energy, and diffusion of atoms; and n is the coarsening exponent whose value determines the mechanism controlling the growth, *i.e.*, volume diffusion (0.33),[42,43] grain boundary diffusion (0.25),[44] or diffusion through dislocations (0.2).[44] Figure 12 shows a log-log plot of average cementite size as a function of holding time during tempering of DP_M steel. Because nonisothermal tempering involves rapid heating, holding time was considered the time required by the specimen to reach the peak temperature (Figure 1), as reported in earlier work.[7,23] As a general prediction of coarsening theory, a power law relationship was clearly seen from the straight line plot with the slope being the coarsening exponent, *i.e.*, n in Eq. [2]. It should be noted that the linear regression fit of the data points was very good with a high regression coefficient value ($R = 0.987$). The n value from the plot was found to be 0.198, on average, suggesting that the coarsening kinetics is dominated by diffusion of solute through dislocations, other than by conventional volume diffusion control.[12,42,43] The present result is supported by

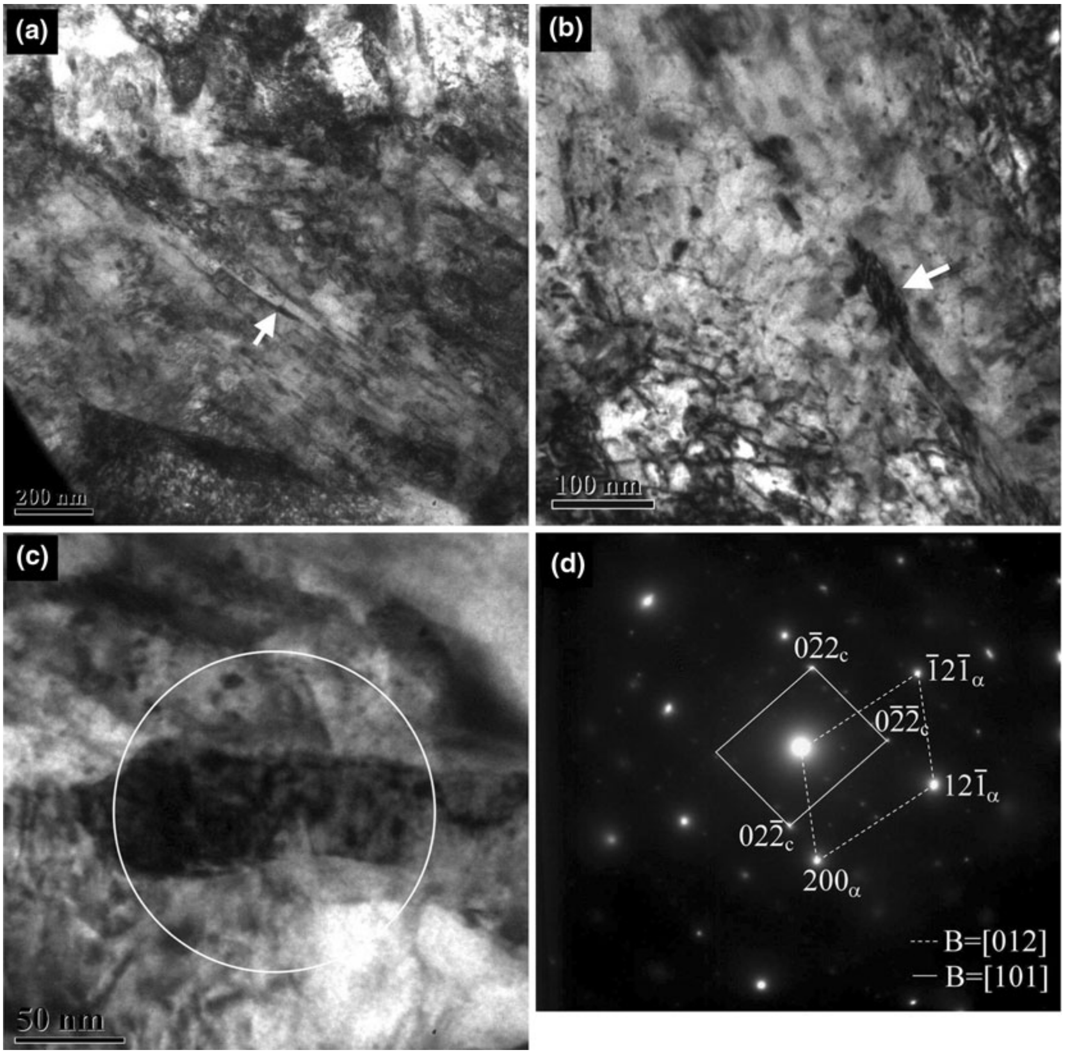

Fig. 9—BF image showing (*a*) cementite along the lath boundaries, (*b*) detailed morphology of intralath cementite, and (*c*) high-magnification image of (b). (*d*) The diffraction pattern of (c) confirming orthorhombic cementite.

Table III. Comparison of Average Size of the Cementite Precipitated at Different Locations in Tempered DP_M Steel

	DP_M Steel Average Cementite Size (nm)			
	Within Block		High-Angle Boundaries	
Tempering Condition	Dislocations	Low-Angle Boundaries	Block Boundaries	Prior Austenite Grain Boundaries
Isothermal (5400 s)	113 ± 37		231 ± 33	224 ± 35
Nonisothermal	intralath 21 ± 10	interlath 23 ± 7	51 ± 15	42 ± 13

the earlier report on growth kinetics of Fe-C alloy at 690 °C, which demonstrated that coarsening of cementite is controlled by diffusion along the dislocation for low carbon containing martensite (0.2 wt pct),[41] close to the martensite carbon content of the DP_M steel (Table II). The coarsening mechanism was further affirmed by the microstructure, illustrating high density of precipitated cementite within the matrix (both intralath and interlath cementite) compared to its density at grain boundaries (Figures 4 through 7). However, it may be noted that the cementite particles were larger at grain boundaries than within grains, which can be attributed to the fact that the growth rate is faster at the grain boundary where larger particles grow at the expense of small particles, which acts as a source of carbon.[45] Interestingly, the *n* value (0.198) in

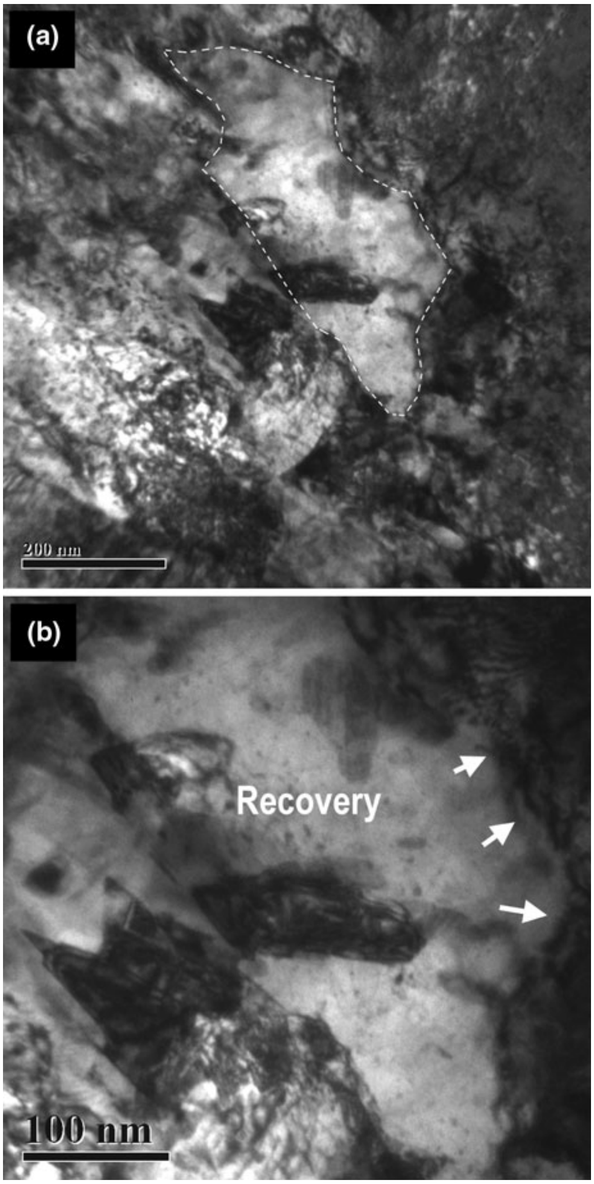

Fig. 10—Partial recovery of the lath substructure in nonisothermal tempering of DP_M steel: *(a)* overview and (*b*) high-magnification image of the recovered region in (a).

the present study was similar to the theoretical value (0.2) despite so many factors that may contribute to any possible deviations: the period in which the coarsening cementite shape is changing from quasi-spherical and elongated (Figure 7) to spherical (Figure 5); the Cr and Mn content in the DP_M steel retarding the coarsening kinetics, decreasing the *n* value;[12,46] and the difference in the extent of recovery over holding time. Lindsley and Marder[41] noted that the ferrite grain size is also believed to influence the coarsening kinetics, the discussion of which is beyond the scope of the present work. Based on the aforementioned discussion, the conclusion of the earlier section is further consolidated; *i.e.*, as the influence of other factors are insignificant on coarsening kinetics, the major difference between isothermal and nonisothermal tempering remains as holding time.

D. *Softening Behavior of DP Steels*

Vickers microhardness of DP_M steel subjected to nonisothermal and isothermal tempering at 923 K (650 °C) was plotted *vs* tempering temperature (Figure 13(a)). Nonisothermal tempering temperatures experienced at the subcritical HAZ regions were identified by their distances from the Ac_1 line, as reported in our earlier study.[31] The error bars in the plot represent the standard deviation from the average of hardness measurements carried out along a line close to the Ac_1 line (in nonisothermal tempering) and (3×3) matrix of indentations (in isothermal tempering) in the specimens. BM hardness (301 HV) was also included (short dashed line) as a reference in the plot to estimate the extent of softening. A significant difference was clearly observed in the softening behavior of DP_M steel in nonisothermal and isothermal tempering. For example, nonisothermal tempering of the DP_M steel resulted in a hardness drop of about 30 HV (10 pct), whereas a higher hardness drop of 78 HV (26 pct) and 118 HV (39 pct) was measured for isothermal tempering at 923 K (650 °C) for 300 and 5400 seconds, respectively (Figure 13(a)). Such dissimilar softening behavior was associated with the difference in structural changes occurring in α' phase during tempering, which is affected mainly by carbon diffusion as discussed in Section III–C. The difference in structural changes in α' substructure during tempering at high temperature, which strongly influences the softening behavior of DP steel, is clearly explained by the schematic illustration (Figure 11). The extensive degree of softening in isothermally tempered DP_M steel was attributed to spheroidization and coarsening of cementite, and complete recovery of the lath α' substructure (Figure 4). In contrast, precipitation of fine cementite (Figure 7) and partial recovery of the lath substructure (Figure 10) led to less severe softening in nonisothermally tempered DP_M steel.

The effect of DP steel chemistry on softening behavior was best explained by the bar graph comparing normalized softening in the nonisothermally tempered DP_L, DP_M, and DP_R steels (Figure 13(b)). To minimize the influence of different fractions of α' in the DP steels, softening was normalized with respect to the volume fraction of martensite in the BM. Normalized softening in HV was calculated as

$$\text{Normalized softening}(HV) = \frac{(H_{BM} - H_{\text{HAZ}})}{f_m} \qquad [3]$$

where H_{BM} is the BM hardness, H_{HAZ} is the hardness of the HAZ, and f_m is the volume fraction of martensite in the respective BM.

The structural details of all the DP steels and the nonisothermally tempered specimens are listed in Table IV.[32] The finer carbides in DP_R steel (Table IV) were associated with the higher carbon content leading to the twinned substructure of α' phase, further confirming that the tempering characteristic of α' in DP steel is similar to that of martensitic steel with similar carbon content.[47] EDX analysis suggested that the substitutional composition of precipitated cementite in nonisothermal tempering is related to the richness of that

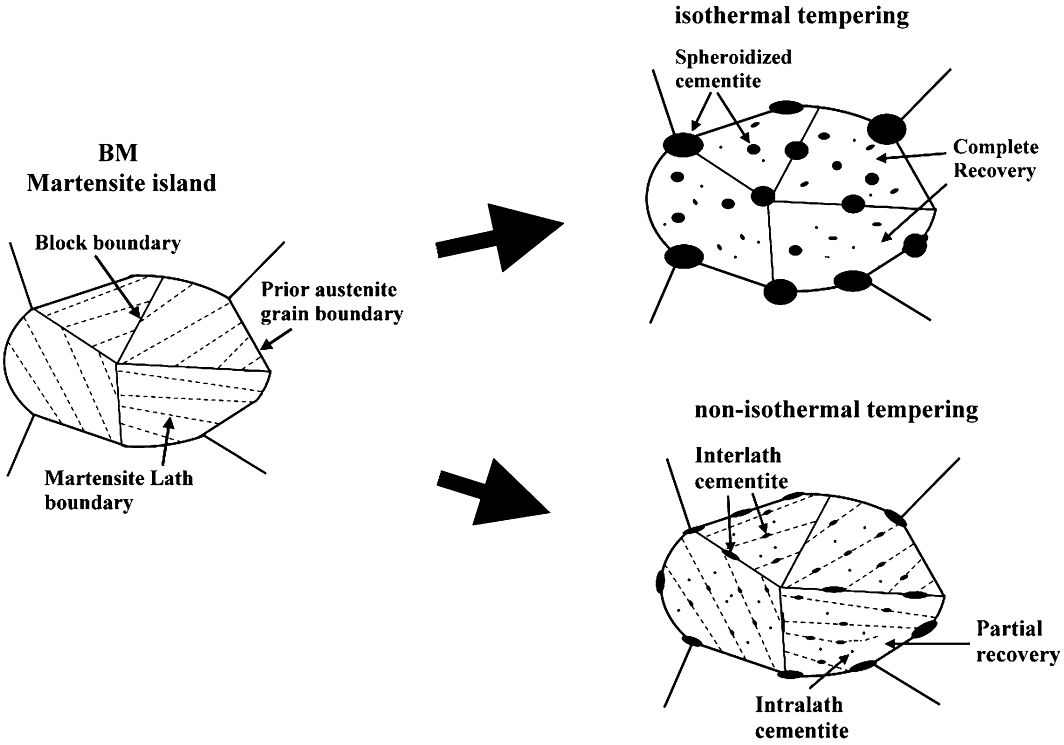

Fig. 11—Schematic illustration showing the differences in the substructure of the martensite phase in DP steel subjected to isothermal and non-isothermal tempering.

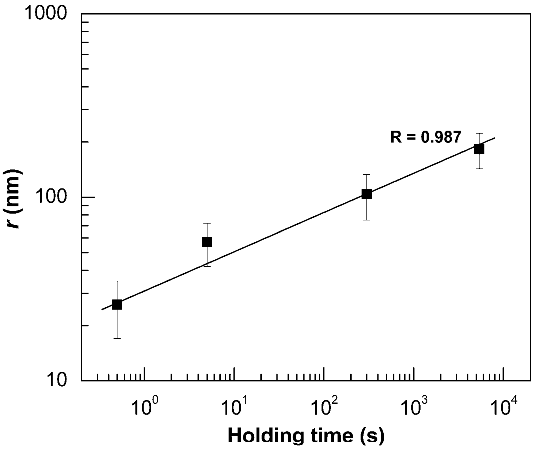

Fig. 12—Cementite growth kinetics at 923 K (650 °C) illustrated by the log-log plot of tempering time *vs* average cementite size for DP_M steel.

particular DP steel chemistry (Table V). For example, cementite of DP_R steel comprised high Cr and Mn content, suggesting precipitation of substitutional rich cementite consistent with the bulk chemical composition of richer DP steel (Table I). The presence of Mn and Cr substitutionals in cementite precipitated in nonisothermally tempered DP steels suggested that thermodynamically stable cementite adopts the stoichiometric form of M_3C (M = Fe, Mn, Cr) consistent with the earlier reports.[12,14,48,49]

Figure 13(b) suggested a trend in the extent of softening similar to that of the cementite size (Table IV), *i.e.*, DP_L (high) → DP_M → DP_R (low). Furthermore, the normalized softening suggested that DP steel of rich chemistry has higher resistance to softening in nonisothermal tempering. This observation was supported well by recent studies on the softening kinetics of DP steels subjected to nonisothermal tempering (laser welding), indicating higher resistance to softening in DP steel of richer chemistry.[7,23] The higher resistance to softening of DP_R steel observed in Figure 13(b) was in accordance with the fine cementite and less decomposed structure of TM, whereas substantial softening in the DP_L steel was related to the coarser cementite and severely decomposed structure of TM (Table IV). Furthermore, the softening is affected strongly by the recovery process of martensite, which is controlled through the growth of lath boundary cementite.[40] Thus, it was concluded that the larger extent of partial recovery of α' substructure in DP_L steel (larger cementite) compared to that in DP_M and DP_R steels resulted in higher softening of lean chemistry DP steel subjected to nonisothermal tempering (RSW). To generalize the conclusion, DP steel with rich chemistry has a high resistance to softening irrespective of the welding process, per the aforementioned discussion for RSW and the recent studies on softening kinetics in the subcritical HAZ of laser-welded DP steels,[23] which reported that carbide forming elements such as Cr and Mo increase the resistance to softening.

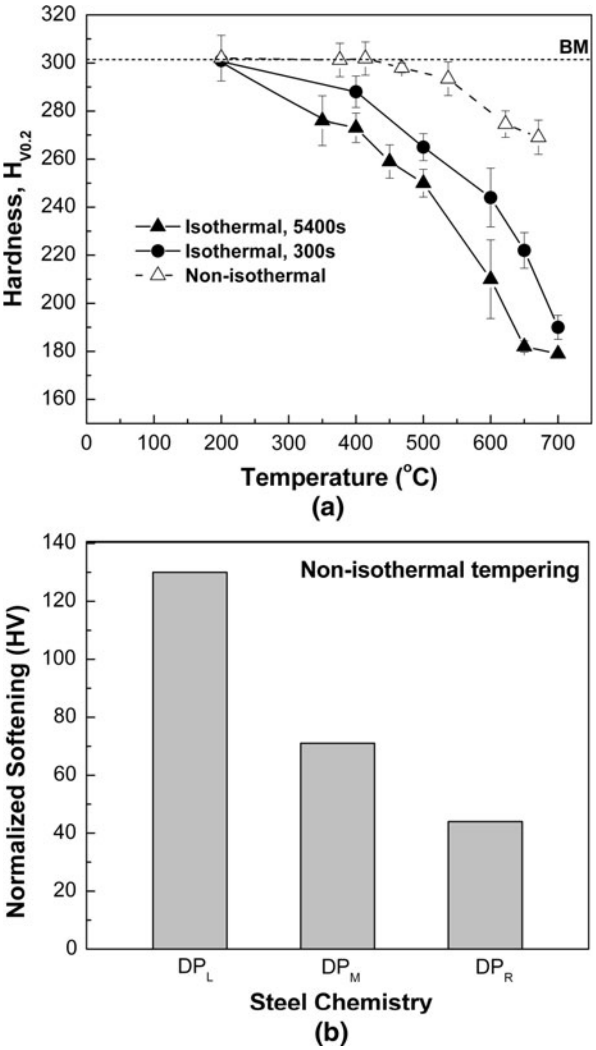

Fig. 13—Softening of DP steels: (*a*) Vickers microhardness of DP_M steel *vs* tempering temperature subjected to nonisothermal and isothermal tempering for 300 and 5400 s, and (*b*) comparison of normalized softening of the all the DP steels in nonisothermal tempering.

Table IV. Comparison of Structural Details of BM and Tempered Specimens of Non-Isothermally Tempered DP Steels

Steel	BM-α' Morphology	Tempered Structure	Cementite Size (nm)
DP_L	laths	severely decomposed	300
DP_M	laths	broken laths	50
DP_R	twins	broken lath	40

Table V. EDX Analysis of Precipitated Cementite in Nonisothermally Tempered DP Steels

Steel	Fe (Wt Pct)	Mn (Wt Pct)	Cr (Wt Pct)
DP_L	99	1	—
DP_M	74	20	6
DP_R	70	12	18

IV. CONCLUSIONS

The morphology of the martensite phase in DP steels studied was dependent on its carbon content: DP_L and DP_M steel contained α' laths (<0.273 wt pct), whereas DP_R steel (~0.360 wt pct) contained twinned structure. Higher Mn content in DP_M steel resulted in interlath retained austenite.

The isothermal tempering of α' in DP_M steel was characterized by coarsening and spheroidization of cementite and complete recovery of the lath substructure, suggesting similar tempering characteristics of DP steel and martensitic steel with similar carbon content.

Fine cementite in nonisothermally tempered DP_M steel, unlike the coarser and spheroidized cementite in isothermal tempering, was attributed to the synergistic effect of delay in cementite precipitation and insufficient time for diffusion of carbon due to the higher heating rate that retards the third stage of tempering (cementite coarsening and recrystallization).

Precipitation of cementite was dominated by diffusion of carbon atoms into lattice defects (dislocations, lath boundaries, block boundaries, and prior-γ grain boundaries), whereas the coarsening mechanism was dislocation diffusion controlled. The precipitated cementite in nonisothermal tempering adopted a stoichiometric form of M_3C (M = Fe, Mn, Cr) type cementite, where its substitutional content is correlated to the richness of the steel chemistry.

The finer cementite and interlath elongated cementite, formed by decomposition of retained austenite, helped in partial recovery of α'-lath substructure due to the pinning effect leading to retardation of lath boundary migration in nonisothermal tempering.

Fine interlath platelike cementite and partial recovery of lath substructure in nonisothermal tempering resulted in low softening compared to severe softening in isothermal tempering due to large spheroidized cementite and complete recovery of the lath structure.

The extent of softening was also found to depend on the chemistry (Cr and Mn content) of DP steel: fine cementite and less decomposed tempered structure of richer chemistry enhanced the resistance to softening compared to severely decomposed martensite in lean chemistries with coarser cementite.

ACKNOWLEDGMENTS

This work was supported by Auto21 (one of the Networks of Centres for Excellence supported by the Canadian Government), The Initiative for Automotive Manufacturing Innovation (IAMI) supported by the Ontario Government, International Zinc Association (IZA) at Belgium, Arcelor Mittal Dofasco at Hamilton, and Huys Industries in Canada. VHBH acknowledges the support from CONACYT Mexico and the Autonomous University of Zacatecas Mexico. The authors are thankful to Professor Scott Lawson, the Centre for Advanced Materials Joining, University of Waterloo, for his constructive comments and suggestions.

REFERENCES

1. Committee on Automotive Applications: *Advanced High Strength Steel (AHSS) Application Guidelines*, International Iron and Steel Institute, Middletown, Ohio, 2009, Version 4.1, pp. 1–4.
2. P.K. Ghosh, P.C. Gupta, R. Avtar, and B.K. Jha: *ISIJ Int*., 1990, vol. 30, pp. 233–40.
3. M. Marya, K. Wang, L.G. Hector, Jr., and X. Gayden: *J. Manuf. Sci. Eng*., 2006, vol. 128, pp. 287–98.
4. R. Neugebauer, S. Scheffler, R. Poprawe, and A. Weisheit: *Prod. Eng*., 2009, vol. 3 (4–5), pp. 347–51.
5. N. Sreenivasan, M. Xia, S. Lawson, and Y. Zhou: *J. Eng. Mater. Technol*., 2008, vol. 130, pp. 041004-1–9.
6. S.K. Panda, N. Sreenivasan, M.L. Kuntz, and Y. Zou: *J. Eng. Mater. Technol*., 2008, vol. 130, pp. 041003-1–9.
7. M. Xia, E. Biro, Z. Tian, and Y. Zhou: *ISIJ Int*., 2008, vol. 48, pp. 809–14.
8. V.H. Baltazar Hernandez, M.L. Kuntz, M.I. Khan, and Y. Zhou: *Sci. Technol. Weld. Join*., 2008, vol. 13, pp. 769–76.
9. M.I. Khan, M.L. Kuntz, and Y. Zhou: *Sci. Technol. Weld. Join*., 2008, vol. 13 (1), pp. 49–59.
10. E. Biro and A. Lee: *AWS Sheet Metal Welding Conf. XI*, Livonia, MI, 2004, paper 5.2.
11. G.B. Olson and W.S. Owen: *Martensite*, ASM INTERNATIONAL, Metals Park, OH, 1992, p. 261.
12. G. Miyamoto, J.C. Oh, K. Hono, T. Furuhara, and T. Maki: *Acta Mater*., 2007, vol. 55, pp. 5027–38.
13. J. Chance and N. Ridley: *Metall. Trans. A*, 1981, vol. 12A, pp. 1205–13.
14. R.C. Thomson and M.K. Miller: *Acta Mater*., 1998, vol. 46, pp. 2203–13.
15. D.L. Williamson, R.G. Schupmann, J.P. Materkowski, and G. Krauss: *Metall. Trans. A*, 1979, vol. 10A, pp. 379–82.
16. M. Sarikaya, A.K. Jhingan, and G. Thomas: *Metall. Trans. A*, 1983, vol. 14A, pp. 1121–33.
17. G. Thomas: *Metall. Trans. A*, 1978, vol. 9A, pp. 438–50.
18. G.R. Speich and W.C. Leslie: *Metall. Trans*., 1972, vol. 3, pp. 1043–53.
19. R.A. Grange, C.R. Hribal, and L.F. Porter: *Metall. Trans. A*, 1977, vol. 8A, pp. 1775–85.
20. R.N. Caron and G. Krauss: *Metall. Trans*., 1972, vol. 3, pp. 2381–89.
21. T. Maki, S. Morito, and T. Furuhara: *Including Steel Heat Treating in the New Millennium, 19th ASM Heat Treating Society Conf. Proc*., ASM International, Cincinnati, OH, Nov. 1–4, 1999, pp. 631–37.
22. N. Farabi, D.L Chen, J. Li, Y. Zhou, and S.J. Dong: *Mater. Sci. Eng. A*, 2010, vol. 527, pp. 1215–22.
23. E. Biro, J.R. McDermid, J.D. Embury, and Y. Zhou: *Metall. Mater. Trans. A*, 2010, vol. 41A, pp. 2348–56.
24. T. Furuhara, K. Kobayashi, and T. Maki: *ISIJ Int*., 2004, vol. 44, pp. 1937–44.
25. A. Nagao, K. Hayashi, K. Oi, S. Mitao, and N. Shikanai: *Mater. Sci. Forum*, 2007, vols. 539–543, pp. 4720–25.
26. S. Tae Ahn, D.S. Kim, and W.J. Nam: *J. Mater. Process. Technol*., 2005, vol. 160, pp. 54–58.
27. N. Yurioka, H. Suzuki, S. Ohshita, and S. Saito: *Weld. J.,* 1983, June, pp. 147–53.
28. I.A. EI-Sesy and Z.M. EI-Baradie: *Mater. Lett*., 2002, vol. 57, pp. 580–85.
29. P. Messien, J.-C. Hernan, and T. Gréday: *Fundamentals of Dual-Phase Steels*, Proc. Symp., TMS-AIME, Warrendale, PA, 1981, pp. 161–80.
30. W. F. Smith and J. Hashemi: *Foundations of Materials Science and Engineering*, 4th ed., McGraw-Hill, New York, NY, 2006, p. 363.
31. V.H. Baltazar Hernandez, S.K. Panda, Y. Okita, and Y. Zhou: *J. Mater. Sci*., 2010, vol. 45, pp. 1638–47.
32. V.H. Baltazar Hernandez: Ph.D. Thesis, University of Waterloo, Waterloo, 2010.
33. T. Maki, K. Tsuzaki, and I. Tamura: *Trans. ISIJ*, 1980, vol. 20, pp. 207–14.
34. G. Tomas: *Metall. Trans*., 1971, vol. 2, pp. 2373–85.
35. G.R. Speich: *Fundamentals of Dual-Phase Steels*, Proc. Symp, TMS-AIME, Warrendale, PA, 1981, p. 16.
36. M.K. Miller, P.A. Beaven, and D.W. Smith: *Metall. Trans. A*, 1981, vol. 12A, pp. 1197–1204.
37. G.R. Speich: *Trans. AIME*, 1969, vol. 245, pp. 2553–64.
38. K.T. Aust and J.W. Rutter: *Grain Boundary Migration, Recovery and Recrystallization of Metals*, American Institute of Mining, Metallurgical and Petroleum Engineers, New York, 1963, pp. 133–69.
39. F.G. Wei and K. Tsuzaki: *Acta Mater*., 2005, vol. 53, pp. 2419–24.
40. S. Takaki, S. Iizuka, K. Tomimura, and Y. Tokunaga: *Mater. Trans. JIM*, 1991, vol. 32, pp. 207–13.
41. B.A. Lindsley and A.R. Marder: *Acta Mater*., 1998, vol. 46, pp. 341–51.
42. I.M. Lifshitz and V.V. Slyosov: *J. Phys. Chem. Solids*, 1961, vol. 19, pp. 35–50.
43. C. Wagner: *Z. Elektrochem*., 1961, vol. 65, pp. 581–91.
44. A.J. Ardell: *Acta Metall*., 1972, vol. 20, pp. 601–09.
45. M.V. Speight: *Acta Metall*., 1968, vol. 16, pp. 133–35.
46. Z.Q. Lv, S.H. Sun, Z.H. Wang, M.G. Qv, P. Jiang, and W.T. Fu: *Mater. Sci. Eng. A*, 2008, vol. 489, pp. 107–12.
47. A. Joarder, J.N. Jha, S.N. Ojha, and D.S. Sharma: *Mater. Characterization*, 1990, vol. 25, pp. 199–209.
48. X. Huang and N.H. Pryds: *Acta Mater*., 2000, vol. 48, pp. 4073–82.
49. P. Schaaf, S. Wiesen, and U. Gonser: *Acta Metall. Mater*., 1992, vol. 40, pp. 373–79.